Entanglement detection from conductance measurements in carbon nanotube Cooper pair splitters

Supplemental Information

Bernd Braunecker,[1] Pablo Burset,[1,2] and Alfredo Levy Yeyati[1]

[1]*Departamento de Física Teórica de la Materia Condensada, Condensed Matter Physics Center (IFIMAC), and Instituto Nicolás Cabrera, Universidad Autónoma de Madrid, E-28049 Madrid, Spain*
[2]*Institute for Theoretical Physics and Astrophysics, University of Würzburg, D-97074 Würzburg, Germany*

(Dated: September 15, 2013)

I. DEMONSTRATION OF EQ. (6)

The current flowing out of an ideal CPS originates only from split Cooper pairs, with one electron being transported over the left and one electron over the right QD. This current is, therefore, subjected to the filtering of spin, valley, and energy of *both* QDs, and probing the current *locally* in one QD contains the *nonlocal* information of the filtering effects of both QDs.

Indeed, in this situation, with filters set along the axes $\nu a_\tau, \nu' b_{\tau'}$ ($\nu, \nu' = \pm$) and resonant conditions such that transport is restricted to the selected levels, the density matrix for the outflowing particles takes the form $\rho_{\nu a_\tau, \nu' b_{\tau'}} = P_{\nu a_\tau} P_{\nu' b_{\tau'}} \rho P_{\nu' b_{\tau'}} P_{\nu a_\tau}$, with ρ the density matrix in the absence of spin-valley filtering. Due to the perfect splitting efficiency, the currents through the left and right QD are identical, and we can focus, for instance, on transport through the left QD only. If $\hat{I}_L$ is the spin and valley independent current operator for transport over the left QD, the property $[\hat{I}_L, P_{\nu a_\tau} P_{\nu' b_{\tau'}}] = 0$ ensures that $\langle \hat{I}_L \rangle = \text{Tr}\{P_{\nu a_\tau} P_{\nu' b_{\tau'}} \hat{I}_L \rho P_{\nu' b_{\tau'}} P_{\nu a_\tau}\} = \text{Tr}\{P_{\nu a_\tau} P_{\nu' b_{\tau'}} \hat{I}_L \rho\}$. In the linear response regime we have furthermore $\langle \hat{I}_L \rangle = V G_L$, with G_L the conductance and V the voltage applied to both leads with respect to the superconductor. As a function of both QD gate voltages, G_L is resonant at the level crossing $\nu a_\tau, \nu' b_{\tau'}$. The full amplitude of the transport at this level crossing, denoted by $G_{\nu a_\tau, \nu' b_{\tau'}}$, is obtained by integrating G_L over this resonance. If furthermore the tunneling rates to the QDs are independent of the QD gates, the quantities $\langle P_{\nu a_\tau} P_{\nu' b_{\tau'}} \rangle = G_{\nu a_\tau, \nu' b_{\tau'}} / \sum_{\tilde{\nu}, \tilde{\nu}'} G_{\tilde{\nu} a_\tau, \tilde{\nu}' b_{\tau'}}$ allow to reconstruct the spin correlators due to the identites $(P_{+a_\tau} - P_{-a_\tau}) \otimes (P_{+b_{\tau'}} - P_{-b_{\tau'}}) = (\mathbf{S} \cdot \mathbf{a}_\tau) \otimes (\mathbf{S} \cdot \mathbf{b}_{\tau'})$ and $(P_{+a_\tau} + P_{-a_\tau}) \otimes (P_{+b_{\tau'}} + P_{-b_{\tau'}}) = \mathbb{1} \otimes \mathbb{1}$. As a consequence we obtain Eq. (6) in the main text. The relation between conductances and spin correlators, therefore, follows from the same considerations used in the proposed entanglement tests based on noise measurements [S1, S2].

To further test Eq. (6) and its consequences on entanglement detection under realistic conditions, we have implemented the microscopic numerical calculation. As discussed in the main text, the numerical results give an objective demonstration that Eq. (6) and the conclusions for entanglement detection remain robust.

II. INFLUENCE OF REALISTIC SETUP ON Q

In this part of the supplement we illustrate the influence of the coupling of the CNT to the superconductor and the normal leads on the determination of Q. We provide all parameters used for the tight-binding calculation following Ref. S3. Finally we show how the level energies and the spin projections evolve with the magnetic field.

Figure S1 shows the dependence of Q on the effective coupling strength Γ_S between the superconductor and the CNT. The insets show parts of the conductance maps for the Γ_S values corresponding roughly to the placements of the insets in the plot. For large Γ_S, the level broadening induced by the superconducting contact mixes the Cooper pairs between the QD levels and the conductances are no longer spin projective. This is notable by the similar intensities of all resonances, and corresponds to a strong enhancement of the local distortions discussed in the text. The corresponding values of Q lie well below 2. Small Γ_S, on the other hand, lead to a weak Cooper pair injection amplitude compared with the hybridization through the superconducting region. As a consequence, the resonance crossings turn into anticrossings. The resulting Q values sharply increase beyond $Q = 2\sqrt{2}$ due to strongly distorted spin correlator reconstructions by the nonlocal hybridization processes. At very small Γ_S, the anticrossings of different levels overlap, and the spin correlator reconstruction becomes erratic.

A valid measurement of Q requires Γ_S corresponding to the central inset in the Fig. S1, represented by well-defined level crossing peaks with unequal intensities. The unequal intensities are a result from the spin filtering of the singlet states, such that spin projection axes that are close to parallel suppress the conductance, while projections that are close to antiparallel allow a maximal transmission. Hence unequal, θ dependent peak intensities are a necessary indicator for spin entanglement, and indeed are the basis for the implementation of the Bell test.

The dependence on the tunnel coupling to the normal leads, characterized by a tunneling amplitude Γ_j for $j = L, R$, is represented in Fig. S2. The combination of the Γ_j with Γ_S defines the broadening of the QD levels. Indeed, in the model of Ref. S3 the lateral leads were represented by ideal one-dimensional channels weakly cou-
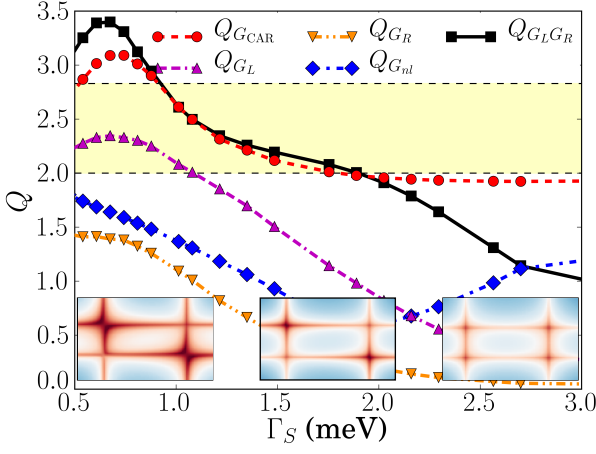
FIG. S1: Dependence of Q on the effective coupling Γ_S to the superconductor for a (20,0) CNT with fixed $\Gamma_{L,R} = 27$ meV, $B = 0.5$ T, $\theta = 45°$, $\theta_{CNT} = 28.8°$. The insets show a zoom on the conductance maps for the Γ_S values corresponding to their placement in the figure, with identical logarithmic color scales [see Fig. 3 (a) in the main text]. The center inset represents the valid regime for testing the Bell inequality with well resolved resonances of different intensities, and the absence of notable avoided crossings of the resonance peaks.
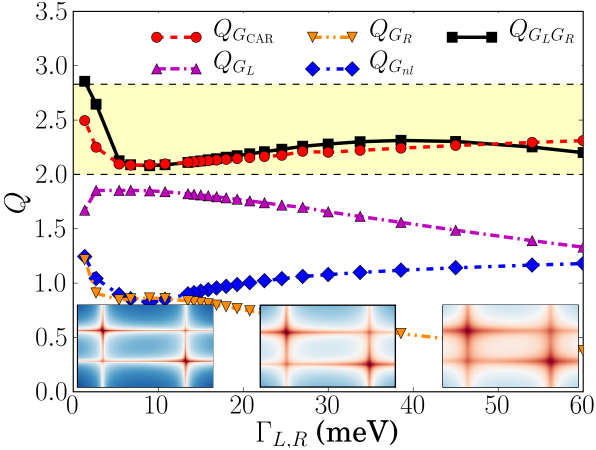

FIG. S2: Dependence of Q on the tunneling amplitudes Γ_j to the normal lead $j = L, R$, for $\Gamma_L = \Gamma_R$ for a (20,0) CNT with fixed $\Gamma_S = 1.35$ meV, $B = 0.5$ T, $\theta = 45°$, $\theta_{CNT} = 28.8°$. The insets show a zoom on the conductance maps for the Γ_j values corresponding to their placement in the figure, with identical logarithmic color scales [see Fig. 3 (a) in the main text]. The center inset represents the valid regime for testing the Bell inequality with well separated resonances and a high enough pixel resolution such that the integral weight of each peak can be determined with high accuracy.

pled to each end site of the nanotube. In the present calculations the tunneling rates to these leads Γ_j take values between 10 and 100 meV. The actual broadening introduced to the QD levels becomes then on the order of $\Gamma_j a/W_j$ with W_j the length of QD j and a the lattice constant.

In contrast to Γ_S, the insets in Fig. S2 show that Γ_j contributes only to a broadening of the levels but leaves the inequality of the peaks unchanged. The Γ_j values of the insets correspond again roughly to the positions of the insets. At large Γ_j, the level overlaps lead to strong local overlaps of the projections such that the Q_{G_j} strongly decrease. Since, however, the unequal intensities and so the spin-filtering properties of each QD level are maintained, the value of Q_{CAR} remains large even for large Γ_j. Yet for larger Γ_j the influence of the overlaps is well notable by the split off of $Q_{G_L G_R}$ from the Q_{CAR} value. For small Γ_j we notice that most conductances lead to an upturn of Q. This effect is attributable to the finite resolution of the peaks from the numerics that become only a few pixels wide, and the result is strongly susceptible to the discretization steps of the V_j. The artificial nature of the low Γ_j behavior is indeed seen by the comparison of Q_{G_L} and Q_{G_R}, which show an anomalous opposite behavior in a regime where all resonances are well separated and all couplings to the left and right QDs are identical. Finally, we notice that since the Γ_j mainly influence the QD levels locally, an asymmetry $\Gamma_L \neq \Gamma_R$ has only little impact on the value of Q as long as all levels can be well resolved.

The results shown in the main text represent the optimal values for the chosen CNT and geometry, $\Gamma_S = 1.35$ meV and $\Gamma_L = \Gamma_R = 27$ meV, determined by first identifying a valid Γ_S leading to well shaped peaks with modulated intensities, and then optimizing the Γ_j to obtain well resolved resonances. These values, however, are strongly sample and geometry dependent and can be used only as indicative.

For the present calculation we have used a CNT of chirality (20,0) with QD lengths $W_L = W_R = 43$ nm and a length of the central superconducting region of 173 nm. Yet the same behavior of level separations and Q values is found for longer system sizes corresponding to experimental situations. A magnetic field of strength $B = 0.5$ T was applied to each QD region with angles θ on the left QD and angles $\theta + \theta_{CNT}$ on the right QD with respect to the CNT axis, for $\theta_{CNT} = 28.8°$. The SOI strengths α, β and the shift Δk_t^{cv} have been implemented using the values of Refs. S4, S5, and are given by $\alpha = -0.08$ meV $/R$, $\beta = -0.31$ meV $\cos(3\eta)/R$, and $\hbar v_F \Delta k_t^{cv} = -5.4$ meV $\tau \cos(3\eta)/R^2$ with R the CNT radius in nm, $\tau = K, K' = +, -$, and η the chiral angle, $\tan(\eta) = \sqrt{3} N_2/(2N_1 + N_2)$, for a CNT with chiralities (N_1, N_2). For $(N_1, N_2) = (20, 0)$ we have $R = 0.78$ nm, $\alpha = -0.10$ meV, and $\beta = -0.40$ meV. The induced superconducting gap is $\Delta = 0.1$ meV, and the doping of the central region -243 meV. All further parameters are as described in Ref. S3. For $(N_1, N_2) = (18, 10)$ as used for Fig. 2 in the main text, we have $R = 0.96$ nm, $\alpha = -0.08$ meV, and $\beta = -0.15$ meV.

Finally, we illustrate the evolution of the QD levels and their spin polarizations as a function of the magnetic field B. Figure S3 displays the 4 spin polarized QD levels of the (18,10) CNT model used for Fig. 2 in the main
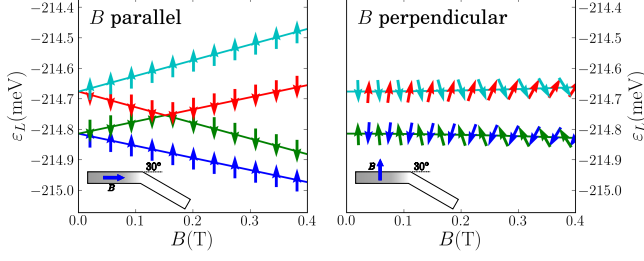
FIG. S3: Levels and spin projections of the left QD as a function of parallel and perpendicular magnetic fields B for the (18,10) CNT described in Fig. 2 of the main text. The sketches in the lower left corners indicate the B field directions with respect to the left QD. The arrows indicate the spin projections in the (x,z) plane with the S^z direction pointing upwards and the S^x direction to the right in the plots. At $B = 0$ the levels of both valleys are degenerate. At increasing B, the levels of one valley increase and the levels of the other valley decrease in energy by the combined effect of orbital and Zeeman fields. At parallel field, the spins remain parallel to the CNT axis. At perpendicular field, the level energies are only weakly affected by B, yet the spin projections in each valley strongly rotate. The situations at $B = 0.4$ T correspond to the selected angles $\theta = 0°, 90°$ in the upper right panel of Fig. 2 in the main text.
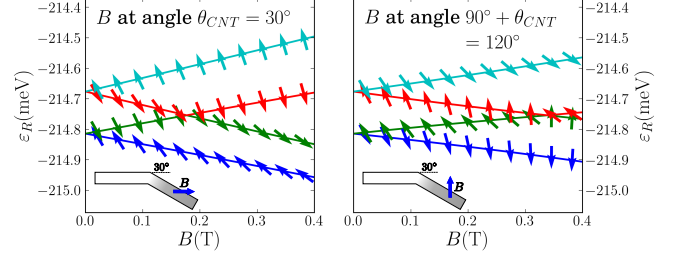
FIG. S4: Levels and spin projections as in Fig. S3 for the right QD at the angle $\theta_{CNT} = 30°$ to the left QD. The sketches in the lower left corners indicate the B field directions with respect to the right QD. The spins are shown in the global (x,z) basis corresponding to Fig. S3. The situations at $B = 0.4$ T correspond to the selected angles $\theta = 0°, 90°$ in the lower right panel of Fig. 2 in the main text.

text, for magnetic fields parallel and perpendicular to the CNT axis of the left QD, respectively. Figure S4 shows the levels of the right QD for the same fields, which are seen for this QD under the additional angle $\theta_{CNT} = 30°$.

[S1] G. B. Lesovik, T. Martin, and G. Blatter, Eur. Phys. J. B **24**, 287 (2001); S. Kawabata, J. Phys. Soc. Jpn. **70**, 1210 (2001).

[S2] N. M. Chtchelkatchev, G. Blatter, G. B. Lesovik, T. Martin, Phys. Rev. B **66**, 161320(R) (2002); P. Samuelsson, E.V. Sukhorukov, and M. Büttiker, Phys. Rev. Lett. **91**, 157002 (2003).

[S3] P. Burset, W. Herrera, and A. Levy Yeyati, Phys. Rev. B **84**, 115448 (2011).

[S4] J. Klinovaja, M. J. Schmidt, B. Braunecker, and D. Loss, Phys. Rev. Lett. **106**, 156809 (2011).

[S5] J. Klinovaja, M. J. Schmidt, B. Braunecker, and D. Loss, Phys. Rev. B **84**, 085452 (2011).